DETECTION OF GASEOUS EFFLUENTS FROM AIRBORNE LWIR HYPERSPECTRAL IMAGERY USING PHYSICS-BASED SIGNATURES

DAVID W. MESSINGER

Digital Imaging and Remote Sensing Laboratory, Chester F. Carlson Center for Imaging Science, Rochester Institute of Technology,
54 Lomb Memorial Dr, Rochester, NY 14623, USA
messinger@cis.rit.edu

CARL SALVAGGIO

Digital Imaging and Remote Sensing Laboratory, Chester F. Carlson Center for Imaging Science, Rochester Institute of Technology,
54 Lomb Memorial Dr, Rochester, NY 14623, USA
salvaggio@cis.rit.edu

NATALIE M. SINISGALLI

Digital Imaging and Remote Sensing Laboratory, Chester F. Carlson Center for Imaging Science, Rochester Institute of Technology,
54 Lomb Memorial Dr, Rochester, NY 14623, USA
nms7102@cis.rit.edu

Detection of gaseous effluent plumes from airborne platforms provides a unique challenge to the remote sensing community. The measured signatures are a complicated combination of phenomenology including effects of the atmosphere, spectral characteristics of the background material under the plume, temperature contrast between the gas and the surface, and the concentration of the gas. All of these quantities vary spatially further complicating the detection problem. In complex scenes simple estimation of a "residual" spectrum may not be possible due to the variability in the scene background. A common detection scheme uses a matched filter formalism to compare laboratory-measured gas absorption spectra with measured pixel radiances. This methodology can not account for the variable signature strengths due to concentration path length and temperature contrast, nor does it take into account measured signatures that are observed in both absorption and emission in the same scene. We have developed a physics-based, forward model to predict in-scene signatures covering a wide range in gas / surface properties. This target space is reduced to a set of basis vectors using a geometrical model of the space. Corresponding background basis vectors are derived to describe the non-plume pixels in the image. A Generalized Likelihood Ratio Test is then used to discriminate between plume and non-plume pixels. Several species can be tested for iteratively. The algorithm is applied to airborne LWIR hyperspectral imagery collected by the Airborne Hyperspectral Imager (AHI) over a chemical facility with some ground truth. When compared to results from a clutter matched filter the physics-based signature approach shows significantly improved performance for the data set considered here.

Keywords: hyperspectral; longwave infrared; gaseous effluent; detection

1. Introduction

Airborne hyperspectral imagery in the longwave infrared (LWIR) provides a useful tool for interrogation of gaseous effluents in the atmosphere. Molecular gases typically exhibit unique spectral absorption features in this spectral regime (8 – 12 μm) allowing for both detection and species identification given a sensor with an appropriate spectral response. However, the physics underlying the at-sensor signature phenomenology is complicated and exploitation of such imagery to detect and characterize gaseous effluents is challenging. Under some circumstances a "residual spectrum" can be computed by measuring or estimating the background spectrum and simply removing this signature from the on-plume measurement. This methodology is not possible for many realistic scenarios such as measurements in a complex industrial facility where there are many materials in the background and the spatial/spectral variability of the background is high. Detection in these scenarios requires a target signature that is well matched to the at-sensor radiance measurement. Such a methodology is presented here.

Detection of plumes in hyperspectral imaging applications has been previously studied. Ifarraguerri (1998)[1] describes a passive standoff chemical agent detection system in which Principle Components Analysis (PCA) and Convex Cone Analysis are used to detect plume pixels in the scene. The Projection Pursuit algorithm has been developed by Ifarraguerri & Chang (1998)[2] for unsupervised detection of gaseous plumes. They show that in a LWIR hyperspectral imager, an SF_6 plume is readily detectable in "early" projections. Matched filter detection of weak gas plumes was investigated by Funk, et al. (2001)[3] on synthetic data. They show that the signal-to-clutter ratio is increased using a modified *k*-means clustering algorithm that in turn improves the matched filter detection. Recently, Foy & Theiler (2004)[4] considered Independent Component Analysis (ICA) as a method of detecting plumes in passive hyperspectral and active LIDAR imagery. They show that it can be effective for weak plumes in characterizing the background clutter and thus improves the ability of matched filters to detect the plume pixels. All of these methods rely on the statistical differences in the scene and do not account for the physics of the target signatures.

Gittins & Marinelli (1998)[5] describe the AIRIS system used for standoff detection of chemical agents. The AIRIS sensor is typically deployed as a ground-based sensor staring across a field of regard allowing for an accurate estimate of the background radiance to be made. Thus, a residual spectrum can be estimated and matched to known gas target species laboratory-measured spectra[6]. Cosofret, *et al.* (2004)[7] describe how the AIRIS system has been used successfully to detect methane leaks in a horizontal viewing geometry with a standoff of as much as 200 m.

The method presented here is based off previous research into the use of physics-based target signatures in a scheme where detection is performed in the native image radiance space. Healey & Slater (1999)[8] and Thai & Healy (2002)[9] first presented the method as a way to overcome deficiencies in atmospheric compensation of visible / near infrared / shortwave infrared (Vis / NIR / SWIR) hyperspectral imagery. In this case, variability in the at-sensor target signature manifestations is modeled through variability in properties of the atmosphere. The method was shown to provide improved detection results particularly for targets in difficult illumination conditions (*i.e.*, in shadow). Ientilucci & Schott (2005)[10] and Ientilucci (2005)[11] extended this method to use a more realistic

forward target model, a more tightly constrained set of input parameters to the forward model, and included the use of an "infeasibility" metric as a false alarm mitigation tool.

These methods were limited to the reflective portion of the electromagnetic spectrum, but have been extended to the LWIR by O'Donnell, *et al.* (2004, 2005)[12,13]. The variability in the target signatures was modeled with variations in the gas concentration and temperature state instead of the atmospheric contributions to the signal. This work used synthetic data over a range of gas temperatures and concentrations and considered both single-species and mixed-species plumes. The research presented here extends this work to application to real LWIR hyperspectral imagery of plumes in a complex, industrial facility.

This paper is presented in the following way. Section 2 describes the phenomenology underlying the at-sensor signature manifestations for pixels affected by the presence of a gas plume and the physics-based model used to predict the target signatures. Section 3 presents the detection algorithm implemented. Section 4 describes the test data used and the detection methodology comparison investigated. Section 5 presents the results from the testing and the paper concludes with a brief summary of the work.

2. Physics-Based Target Model

Typical target detection in visible / near infrared / short-wave infrared (Vis / NIR / SWIR) hyperspectral imagery uses a matched filter formalism[14] where the reflectance spectrum of the target of interest is matched to each pixel in an atmospherically compensated image. This provides good detection results if the image can be accurately transformed into the pixel reflectance space. Another methodology uses physics-based models to predict target signatures in the image radiance space[8,9,10,11]. Here, uncertainties in the atmospheric and illumination conditions on a per-pixel basis are built into a forward model predicting not one, but several target manifestations in the image radiance space. In this manner, a target sub-space is built up describing the possible target signatures in the image. This space is reduced through either statistical or geometric methods[15] to a set of basis vectors or end-member spectra. The background space of the image is similarly characterized and every pixel is tested as to whether it is more "like" the background space or more "like" the target space. In this manner, a likelihood map of target detections can be created.

This physics-based signature detection methodology has been applied here to the detection of gaseous effluents in longwave infrared (LWIR) imagery[12,13]. Here, the variability in the at-sensor signature is not based in illumination and atmospheric uncertainties, but rather in the gas concentration path length and temperature contrast with the surface. For any release, these physical parameters will vary spatially within the scene and thus, a matched filter detection scheme with a single target spectrum may not be optimal.

The longwave infrared spectral regime is dominated by thermal emission from both solid surfaces and the atmosphere. Gas plumes can be detected through their unique spectral absorption and emission characteristics. The absorption spectrum of a gas can be measured in the laboratory[16]. Such signatures determine the "location" of the spectral signature of gases, but not the magnitude or "direction" (*i.e.*, whether the gas feature is

observed in emission of absorption). These are determined by the gas concentration path length and the temperature contrast between the column of gas and the surface beneath the column. For an observed pixel that does not contain the effects of a gas plume, the at-sensor radiance can be approximated as

$$L(\lambda) = \varepsilon_s(\lambda) B(\lambda, T_s) \tau_{atm}(\lambda) + L_u(\lambda) \quad (1)$$

where $L(\lambda)$ is the measured radiance as a function of wavelength λ, $\varepsilon_s(\lambda)$ is the surface spectral emissivity, $B(\lambda,T_s)$ is the Planckian blackbody radiance for the surface at a temperature T_s, $\tau_{atm}(\lambda)$ is the atmospheric transmission, and $L_u(\lambda)$ is the atmospheric upwelling radiance. Atmospheric downwelling radiance that is reflected off the surface is ignored and the surface pixel is assumed to have only a single material at constant temperature.

The at-sensor signature of a pixel containing the effects of a layer of gaseous effluent containing a single species can be approximated in the following way. We write the at-sensor measured radiance as

$$L(\lambda) = \left\{ \varepsilon_s(\lambda) B(\lambda, T_s) \tau_g(\lambda) + \varepsilon_g(\lambda) B\left(\lambda, T_g\right) \right\} \tau_{atm}(\lambda) + L_u(\lambda) \quad (2)$$

where subscripts g refer to the gas plume quantities. Further simplifications can be made. The gas emissivity can be related to the concentration path length of the gas and the absorption coefficient of the gas species by

$$\varepsilon_g(\lambda) \approx ck(\lambda). \quad (3)$$

Here the units of c are parts-per-million-meter (ppm-m) and the units of $k(\lambda)$ are 1/[ppm-m]. Additionally, for optically thin gas layers, the gas transmission can be approximated as

$$\tau_g(\lambda) = 1 - \varepsilon_g(\lambda). \quad (4)$$

These simplifications lead to a radiance model of a pixel containing a layer of gas that can be written as

$$L(\lambda) = \left\{ \varepsilon_s(\lambda) B(\lambda, T_s)(1 - ck(\lambda)) + ck(\lambda) B\left(\lambda, T_g\right) \right\} \tau_{atm}(\lambda) + L_u(\lambda). \quad (5)$$

Re-arranging terms in this model demonstrates some signature phenomenology that leads to the physics-based signature detection approach for the gas detection problem. If the at-sensor radiance is written as

$$L(\lambda) = \left\{ \varepsilon_s(\lambda) B(\lambda, T_s) + ck(\lambda) \left[B\left(\lambda, T_g\right) - \varepsilon_s(\lambda) B(\lambda, T_s) \right] \right\} \tau_{atm}(\lambda) + L_u(\lambda) \quad (6)$$

we see that the signature strength of the gas depends on several factors. First, there will only be unique signatures in spectral regions where the gas has absorption / emission features as measured in $k(\lambda)$. Outside these spectral regions, the gas is transparent. Second, the magnitude of the signature is dependent on two factors. The concentration path length of the gas, c, scales the overall signature strength as long as the concentration is low enough that the gas is optically thin. Also, the temperature contrast between the layer of gas and the surface below the layer is of dramatic importance as it not only influences the "strength" of the feature, but also the "shape" of the feature. One can

easily see from eq. 6 that for pixels where the gas temperature is greater than the effective temperature of the surface, the gas signature will be in emission. In pixels with a lower gas temperature than the surface effective temperature, the gas signature will be in absorption. This also gives rise to the phenomena that for optically thin plumes where the gas temperature is equal to the effective surface temperature, there is *no signature* due to the gas regardless of the concentration path length of the layer. This signature variability based on concentration path length and temperature contrast with the surface motivates a detection scheme that does not search for a single target signature, but many. Downwind from the release point, as the gas cools and diffuses, the signatures may be dramatically different from those near the stack where the concentration and temperature are the greatest.

The previously mentioned radiometric model of a pixel containing a layer of gas is implemented in the detection scheme described here with one further definition. The gas temperature is described explicitly in terms of a temperature contrast with the surface temperature by writing it as

$$T_g = T_s + \Delta T \tag{7}$$

where ΔT is the difference between the surface and gas temperatures. Of course, accurately estimating the surface temperature without knowledge of the surface material emissivity is a problem in and of itself, so an approximate method is used here. The goal in the physics-based signature prediction model is to generate a large number (several hundred) of target signature manifestations that describe (or bound) the possible ways in which the signature could appear in the scene. These manifestations are then searched for in the image and compared with a characterization of the background to contrast each pixel as more "target like" or more "background like".

3. Detection Algorithm

The detection scheme implemented here uses the physics-based model shown in equation 6 to generate a large number of target signature manifestations. The atmosphere is not varied (as was the case in the reflective implementation of this approach[8,9,10,11]). Instead, a single estimate of the atmospheric contributions to the at-sensor signal is used in the forward model. The surface temperature is estimated through the identification of a "background" region of interest assumed to be free of the effects of the gas layer, but representative of the materials in the scene. Over this region, the brightness temperature spectrum, $T_b(\lambda)$ is computed for each pixel by inverting the Planck function for each wavelength in the pixel. The maximum brightness temperature in each pixel $T_{b,max}$ is then compiled into a list, and the mean value of the set of $T_{b,max}$ is computed over the region. This value is used as an estimate to the surface temperature in equation 6. The background material in the forward model is assumed to be a blackbody.

The variability in the predicted radiance signatures derives from computing the signatures over a range of concentration path lengths and ΔT. Typically, the concentration path length is varied from between 0.1 [ppm-m] and 100 [ppm-m], simulating cases of very high and relative low concentrations. ΔT is generally allowed to vary between -10K and +10K. The range of each parameter is subdivided into a fixed number of intervals (10 were chosen in this study). Signatures are then predicted for every combination of

concentration path length and temperature contrast. In this way, signatures are predicted for hot, dense portions of the plume as well as cool, diffuse portions of the plume and a range of possibilities in between.

Once the target space is created, it is reduced to a set of end member spectra using a geometric projection scheme. The Maximum Distance Method (MaxD)[15] is used to determine the extrema spectra that define the convex hull enclosing the data in the space. For this work, the target space was reduced to eight end member spectra. The background is characterized in a similar way. The background region of interest described above is reduced to a set of background end member spectra using the same MaxD procedure as the target space. Here, the background was characterized with 15 end member spectra. Efforts were not made to optimize the background or target space characterizations in terms of the number of end member spectra used to describe the space. Research into this topic is ongoing.

Given the background and target space characterizations, a test is applied to each pixel to determine the likelihood that it contains the effects of the target gas in question. The test used is the Generalized Likelihood Ratio Test, GLRT[15] The GLRT as formulated here is based on the matched subspace detector, MSD, written as

$$MSD(\boldsymbol{x}) = \frac{\boldsymbol{x}^T\left(\boldsymbol{P}_B^{\perp} - \boldsymbol{P}_Z^{\perp}\right)\boldsymbol{x}}{\boldsymbol{x}^T\boldsymbol{P}_Z^{\perp}\boldsymbol{x}} \tag{8}$$

where $\boldsymbol{x}$ is the test pixel vector, and $\boldsymbol{P}_Y^{\perp}$ represents the projection matrix orthogonal to the subspace $\boldsymbol{Y}$. The subscript $\boldsymbol{Z}$ denotes the subspace matrix containing the background space basis vectors augmented with the target space basis vectors and the subscript $\boldsymbol{B}$ represents the background basis vectors. The GLRT is then written as

$$GLR(\boldsymbol{x}) = \left[MSD(\boldsymbol{x}) + 1\right]^{\frac{p}{2}} \tag{9}$$

where p is the number of bands in the pixel spectrum. The use of other detectors within the physics-based signatures scheme is under investigation.

The detection scheme is run iteratively on several gas species of interest for a single scene. Separate target spaces are created for each species using the same input parameters to the signature model and the individual species' laboratory absorption spectrum. As a result, individual detection planes are generated for each target species considered. Mixed plumes are not considered in the detection scheme (*i.e.*, target signatures containing mixtures of gases are not generated and used in the detection process for this study).

4. Test Data

The data used in this study were collected with the Airborne Hyperspectral Imager (AHI) by the University of Hawaii as part of an experiment for the US Environmental Protection Agency. AHI is a longwave infrared (LWIR) pushbroom imager that collects 256 cross-track pixels in 256 spectral channels ranging from 8-11.5 μm[17]. The data collection also used a color infrared (CIR) line scanner producing images for context. Imagery of an industrial facility with known release points was collected during April 2004. Ground truth of the releases consists of the general locations of the releases and the list of species possibly contained in the plumes. No controlled release experiments

were performed. All plumes in the imagery were live releases. As such, exact knowledge of the locations and constituent species is unknown making the declaration of "detections" relatively subjective.

Several flightlines were collected during the flight campaign, including both day and night flights, as well as flights at several altitudes. The data used here were collected during the day and were at an altitude of 5000 ft providing a ground sample distance (GSD) of approximately 2 m. Preprocessing of the data was required to remove known bad bands from the data (*e.g.*, at the beginning and end of the spectral region covered) and image edge effects. The data were not spectrally binned for this application as is sometimes done with AHI data to improve the signal-to-noise ratio. Here, the native spectral resolution of the sensor was used.

For comparison, a simple clutter matched filter was applied to the data as well as the physics-based signatures algorithm. The clutter-matched filter was implemented as

$$CMF(\boldsymbol{x}) = \frac{\boldsymbol{d}^T \Sigma^{-\frac{1}{2}} \boldsymbol{x}}{\boldsymbol{d}^T \Sigma^{-\frac{1}{2}} \boldsymbol{d}} \tag{10}$$

where $\boldsymbol{d}$ is the target spectrum of interest, here taken to be the laboratory-measured gas absorption spectrum, $\boldsymbol{x}$ is the de-meaned pixel under test, and $\boldsymbol{\Sigma}$ is the background covariance. Both the mean and covariance of the background were estimated from the same set of pixels used to characterize the background in the physics-based approach described above (*i.e.*, the background region of interest).

5. Results

The physics-based signature detection scheme was applied to the dataset as described above.
Application of the physics-based signatures detection requires an estimate of the atmospheric contributions to the at-sensor signatures (see eq. 6). Here, the atmosphere used was the MODTRAN mid-latitude summer model[18] for the appropriate sensor altitude, day of the year, and time of day. No attempt was made to optimize the atmosphere for the data. Improvements in the match between the atmosphere used in the target space prediction and that actually contributing to the data should improve the detection results.

Target signatures used were taken from a commercially available database of laboratory-measured absorption spectra[16] and were convolved with the spectral response of the sensor (as were the atmospheric contributions described previously). Target species were determined from the ground truth listing of potential releases provided with the dataset. Species in the target library used were methane, propane, butane, ethane, sulfur dioxide, ethylene, propylene, and benzene.

A region of the facility expected to contain methane and ethane releases was investigated as described above and the results are shown below. The physics-based signatures approach and the clutter-matched filter were applied to this image. Figure 1 shows the CIR image of the area and the corresponding 10.5 μm band from the AHI hyperspectral cube. The region is very cluttered containing several background materials: roads, soils,

several structures, cooling towers, and extensive metal piping. The full detection images for both target species and both methods are also shown.

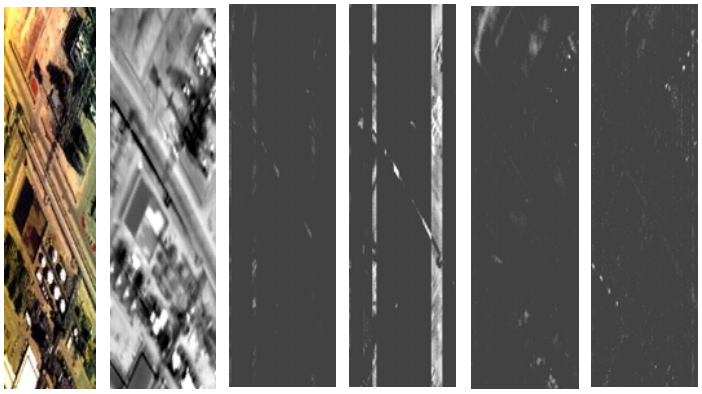

Figure 1: (a) Color IR image of the facility investigated for propane and ethane releases. (b) 10.5 μm band of the corresponding area from the AHI hyperspectral cube. (c) Physics-based signatures detection image for ethane. (d) Physics-based signatures detection for methane. (e) Clutter matched filter detection of ethane. (f) Clutter matched filter detection of methane. The physics-based signature detection images are thresholded to show the top 5% of detection in the image and the clutter matched filter results are thresholded to show the top 10% of detections in the image.

In the full detection images, several features of note are apparent. The clutter matched filter results are highest on the very "bright" objects in the scene. This is a common source of false alarms for this method as it is essentially a projection operator and the test statistic can be large for pixels with a large vector magnitude regardless of spectral similarity to the target spectrum. The physics-based signatures method detects false alarms on two different types of pixels. The diagonal stripe through the center of the detection image corresponds to the surface feature seen in the image. This material may not have been correctly characterized in the background ROI and as such, the detection scheme has difficulty differentiating it from the target space. The vertical stripes correspond to sensor artifacts in the imagery itself. The physics-based method predicts signatures in the radiometric space of the sensor, but here, sensor artifacts or mis-calibrations were not included in the model. Consequently, the manifestations of the targets in these pixels were not correctly predicted and the detection scheme has difficulty distinguishing between target and background. Closer inspection of the physics-based signature detection results show three isolated regions of a high detection statistic outside these regions, described in more detail below (the detections are spatially small making them difficult to distinguish in the full-size images shown in Figure 1). The first is of an ethane release and the remaining two show methane releases. Of particular note is the observation that the physics-based detections are at approximately the same detection level as the false alarms making mitigation relatively simpler. No other species in the target library were detected at appreciable levels.

Figure 2 shows a region highlighting an ethane detection in the physics-based signatures method. The corresponding region in the clutter matched filter detection is also presented

along with the higher resolution CIR image of the area providing scene context of the detection.

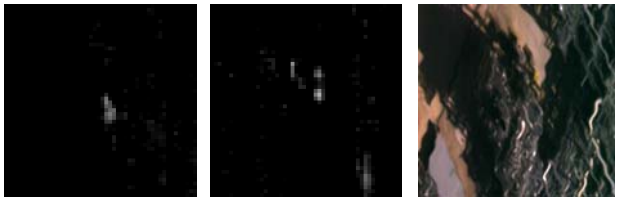

(a) (b) (c)

Figure 2: Zoom of the region showing the ethane detection. (a) Physics-based signatures detection. (b) Clutter matched filter detection. (c) CIR image of region of detection for context. The detection images are perfectly registered (they are based on the same input LWIR image) but the CIR image is not and has a different spatial resolution. The detections are approximately in the center of the CIR image.

Here, the detection using the physics-based signatures algorithm produces a small, compact, plume-shaped object with a conical shape indicative of a source and diffusion downwind. The detection strength across the plume in the physics-based signature result is relatively uniform and continuous. This is in contrast to the clutter matched filter results which, while showing strong detections, are discontinuous and do not exhibit the same spatial characteristics.

Figure 3 shows one of the two methane releases detected in this region of the facility. Again, the clutter matched filter results are shown as well as the higher resolution CIR image to provide scene context. Here, the clutter matched filter results (thresholded to only show the top 10% of all detections) do not show any detection of methane. If the matched filter has detected the plume, it is so far below the highest detections in the image that it is not observable at this level. Similar to the ethane detection above, the plume detected in the physics-based signatures detection scheme is small, compact, and has spatial characteristics indicative of a small release diffusing due to the effects of the local wind.

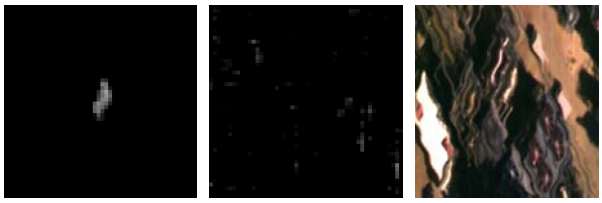

(a) (b) (c)

Figure 3: Zoom of the region showing the first methane detection. (a) Physics-based signatures detection. (b) Clutter matched filter detection. (c) CIR image of region of detection for context. The detection images are perfectly registered (they are based on the same input LWIR image) but the CIR image is not and has a different spatial resolution. The detections are approximately in the center of the CIR image.

Figure 4 shows results for the second methane plume detection with the physics-based signatures detection algorithm. Again, the clutter-matched filter fails to detect any methane at this level while the physics-based signatures algorithm detects a spatially compact, well-defined source.

(a) (b) (c)

Figure 4: Zoom of the region showing the second methane detection. (a) Physics-based signatures detection. (b) Clutter matched filter detection. (c) CIR image of region of detection for context. The detection images are perfectly registered (they are based on the same input LWIR image) but the CIR image is not and has a different spatial resolution. The detections are approximately in the center of the CIR image.

6. Summary

An algorithm for the detection of gaseous effluents from airborne LWIR hyperspectral imagery of complex scenes has been developed based on the use of physics-based signature predictions. This method accounts for the complex phenomenology underlying the gas signatures manifested at the sensor including variations in the gas concentration path length and temperature contrast with the surface. Detection results for imagery of a facility collected with the AHI airborne LWIR hyperspectral sensor have been presented for both the physics-based signatures approach and the more common clutter matched filter. In the latter case, the target spectrum was the laboratory-measured gas absorption spectrum, a common approach used when a "residual" spectrum is easily estimated. Here, due to the complex nature of the scene such an approach is more difficult and the physics-based approach has been shown to outperform the simple matched filter.

While the physics-based approach provides detections where the clutter matched filter does not, it is also important to note the nature of the false alarms generated by each method. The clutter-matched filter is essentially a projection operator and is susceptible to false alarms on pixels with large spectral magnitude (*i.e.*, "bright" pixels). The physics-based approach tends to false alarm on background materials not well characterized and on sensor artifacts. The latter is because the detection is in the native radiance space of the image and in the presence of miscalibration or artifacts, the predicted signatures will not match well with the measurement.

Improvements to the algorithm are under investigation. Incorporation of real background materials in the target model (as opposed to the assumed blackbody used here) could improve performance. Additionally, target and background space characterization, as well as a detection scheme, that uses a geometric model has not been sufficiently proven to be the optimal method for detection of gas plume in LWIR imagery. Other methods, such as unstructured detection schemes will be tested to characterize performance.

Finally, no efforts were made here to optimally estimate the atmospheric contributions to the at-sensor target signature predictions. Use of more accurate estimates of these quantities will better match the target signatures to the measured signatures and should improve performance over that presented here.

Acknowledgements

The authors would like to thank Mr. David Williams of the US Environmental Protection Agency for providing the data used in this study.

References

1. Ifarraguerri, A, Exploitation of imaging spectrometry data for chemical cloud detection, identification and mapping, Proceedings of the 1997 ERDEC Conference on Chemical Defense Research, Special Publication ERDEC-SP-063, 401-406 (1998)
2. Ifarraguerri, A. and Chang, C-I, Projection pursuit analysis of hyperspectral scenes, Conference on Algorithms for Multispectral and Hyperspectral Imagery IV, Proceedings of SPIE, vol. 3372, 1-59 (1998)
3. Funk, C.C., Theiler, J., Roberts, D.A, and Borel, C.C., Clustering to improve matched filter detection of weak gas plumes in hyperspectral thermal imagery*, IEEE Transactions on Geoscience and Remote Sensing*, **39**(7), 410-1420 (2001)
4. Foy, B.R. and Theiler, J., Scene analysis and detection in thermal infrared remote sensing using independent component analysis, Independent Component Analyses, Wavelets, Unsupervised Smart Sensors, and Neural Networks II, Proceedings of SPIE vol. 5439, 131-139 (2004)
5. Gittins, C.M. and Marinelli, W., AIRIS multispectral imaging chemical sensor, Electro-Optical Technology for Remote Chemical Detection and Identification III, Proceedings of SPIE, vol. 3383, 65-74 (1998)
6. Jensen, J.O., Thierault, J-M., Bradette, C., Gittins, C. and Marinelli, W., Results from the pronghorn field test using passive infrared spectroradiometers - CATSI and AIRIS, Algorithms and Technologies for Multispectral, Hyperspectral, and Ultraspectral Imagery VIII, Proceedings of SPIE, vol. 4725, 177-183 (2002)
7. Cosofret, *et al.* Passive infrared imaging sensor for standoff detection of methane leaks, Chemical and Biological Standoff Detection II, Proceedings of SPIE, vol. 5584, 93-99 (2004)
8. Healey, G. and Slater, D., Models and methods for automated material identification in hyperspectral imagery acquired under unknown illumination and atmospheric conditions, *IEEE Transactions on Geoscience and Remote Sensing,* **37**(6), 2706-2717 (1999)
9. Thai, B. and Healey, G., Invariant subpixel material detection in hyperspectral imagery, *IEEE Transactions on Geoscience and Remote Sensing*, **40**(3), 599-608 (2002)
10. Ientilucci, E.J. and Schott, J.R., Target detection in a structured background environment using an infeasibility metric in an invariant space, Algorithms and Technologies for Multispectral, Hyperspectral, and Ultraspectral Imagery XI, Proceedings of SPIE, vol. 5806, 491-502 (2005)
11. Ientilucci, E.J., Hyperspectral subpixel target detection using hybrid algorithms and physics based modeling, Ph.D. thesis, Rochester Institute of Technology (2005)
12. O'Donnell, E.M., Messinger, D.W., Salvaggio, C., and Schott, J.R., Identification and detection of gaseous effluents from hyperspectral imagery using invariant algorithms, Algorithms and Technologies for Multispectral, Hyperspectral, and Ultraspectral Imagery XI, Proceedings of SPIE, vol. 5425, 573-582 (2004)
13. O'Donnell, E.M., Messinger, D.W., Salvaggio, C., and Schott, J.R., The invariant algorithm for identification and detection of multiple gas plumes and weak releases, Algorithms and

Technologies for Multispectral, Hyperspectral, and Ultraspectral Imagery XI, Proceedings of SPIE, vol. 5806, 206-217 (2005)
14. Manolakis, D., Marden, D., and Shaw, G., Hyperspectral image processing for automatic target detection applications, *Lincoln Laboratory Journal*, **14**(1), 79-116 (2003)
15. Bajorski, P., Ientilucci, E.J., and Schott, J.R., Comparison of basis-vector selection methods for target and background subspaces as applied to subpixel target detection, Algorithms and Technologies for Multispectral, Hyperspectral, and Ultraspectral Imagery XI, Proceedings of SPIE, vol. 5425, 97-108 (2004)
16. Sharpe, S., et al., Creation of 0.10 cm^{-1} resolution, quantitative, infrared spectral libraries for gas samples, Vibrational Spectroscopy-Based Sensor Systems, Proceedings of SPIE, vol. 4577, 12-24 (2001)
17. Lucey, P., et al., AHI: An airborne longwave infrared hyperspectral imager, Airborne Reconnaissance XXII, Proceedings of SPIE, vol. 3431, 36-43 (1998)
18. Berk, A., Bernstein, L.S., and Robertson, D.C., MODTRAN: A moderate resolution model for LOWTRAN 7, Air Force Geophysics Laboratory, GL-TR-89-0122 (1988)